

6th CIRP Conference on Surface Integrity

Effect of thermomechanical loads and nanocrystalline layer formation on induced surface hardening during orthogonal cutting of AISI 4140

Germán González^{a,*}, Florian Sauer^a, Marcel Plogmeyer^b,
Michael Gerstenmeyer^a, Günter Bräuer^b, Volker Schulze^a

^awbk Institute of Production Science, Karlsruhe Institute of Technology (KIT), Kaiserstr. 12, 76131 Karlsruhe, Germany

^bTU Braunschweig, Institute for Surface Technology (IOT), Bienroder Weg 54E, 38108 Braunschweig, Germany

* Corresponding author. Tel.: +49-721-608-42455; fax: +49-721-608-45004. E-mail address: german.gonzalez@kit.edu

Abstract

Strain-hardening, thermal-softening as well as grain refinement may lead to unexpected changes in surface hardness of turned steel parts. Although the relationship between hardness, microstructure and cutting parameters has been investigated in previous research works, the prediction of surface hardness remains still a challenge. In this work, orthogonal turning tests were performed using low carbon steel AISI 4140 and thermomechanical loads, surface hardness and microstructure were measured. The relationship between surface hardness and thermomechanical loads was explored by establishing an empirical model. Moreover, grain size evolution was observed and correlated with micro hardness. Results suggest that cutting conditions can be controlled to achieve desired surface hardness by evaluating functions dependent on in-process measurements.

© 2022 The Authors. Published by Elsevier B.V.

This is an open access article under the CC BY-NC-ND license (<https://creativecommons.org/licenses/by-nc-nd/4.0>)

Peer review under the responsibility of the scientific committee of the 6th CIRP CSI 2022

Keywords: white layer; surface hardening; thin-film-sensor

1. Introduction

Surface hardening, also known as work, strain or phase hardening, is an inherent part of the machining process where the generated mechanical and thermal loads are high enough to harden the workpiece. When turning hardenable steels, the surface of the workpiece undergoes high temperature gradients and severe plastic deformations. This lead to the displacement, generation and annihilation of dislocations in the subsurface layers and to changes in the microstructure and therefore in the mechanical properties as hardness as suggested by Kocks & Mecking [1]. The degree of hardening depends on the thermomechanical loads, the properties of the material, such as the content of carbon and other alloying elements. Scrapped parts caused by severe surface deformations due to too high loads and excessive tool wear and tool breakage are the main problems that ignorance of work hardening can cause [2].

The surface layer resulting from the machining process are commonly named white layers, due to their featureless appearance in an optical microscope, consequence of light dispersion at their nanocrystalline structure. As suggested by Hosseini [3], there exist two different types of white layers, thermally and mechanically induced. The first type is formed through an excessive thermal load, which produces dynamic recovery and dynamic recrystallization causing ultrafine grained structures and phase transformations. The second type is formed through the dynamic recovery process at low temperatures where phase transformations do not occur.

The modelling of work hardening still remains a challenge. The surface hardness can be predicted using for instance the Hall-Pech correlation and the grain size [4], which is obtained numerically with models based on dislocation density [5] or on the Zener-Hollomon parameter [6], but they lack precision when subjected to high strain rates, such as in machining.

Nomenclature

| | |
|-------------------|--|
| v_c | cutting speed, m/min |
| f | feed per revolution, mm/rev |
| h | uncut chip thickness, μm |
| r_β | cutting edge radius, μm |
| T_{tfs} | thin film sensor temperature, $^\circ\text{C}$ |
| T_t | tool thermocouple temperature, $^\circ\text{C}$ |
| T_w | workpiece thermocouple temperature, $^\circ\text{C}$ |
| T_z | workpiece temperature at distance z from surface, $^\circ\text{C}$ |
| $Z_{\text{gs}<x}$ | distance z from the surface with a gran size $< x$, μm |
| α_f | ratio between cutting and passive force F_c / F_p , - |

In this work, the surface hardness of orthogonally turned workpieces made of AISI 4140 was examined and modeled with various statistical models. The main goal is the efficient prediction of surface hardness using information that can be collected and processed during the machining process and/or previously generated databases. Finite element models and experimental tests were used to generate the databases. The microstructure of the workpiece is studied using resource-intensive techniques, which mainly lead to a better understanding of the hardening process and validation of the proposed models. The real-time modeling approaches will enable digital process twins with richer information about the surface integrity of the part [7].

2. Material and methods

2.1. Material

All tests were carried out with AISI 4140 steel. Its chemical composition is given in Table 1. Blank samples were quenched and then tempered at 600°C for 1 h according to DIN 10083 to obtain a high content of tempered martensite microstructures that lead to a hardness of 365 HV30. The workpieces were turned to a starting diameter of 49 mm and ground to a thickness of 4 mm.

Table 1. Chemical composition of AISI 4140 steel (wt %).

| C | Si | Mn | P | S | Cr | Mo | V |
|------|------|------|-------|-------|------|-----|-------|
| 0.40 | 0.23 | 0.74 | 0.016 | 0.027 | 1.04 | 0.2 | 0.007 |

2.2. Measurement equipment

In-machine. Cutting forces and temperatures were measured using a tool holder attached to a Kistler© dynamometer type 9257B, in-tool-integrated thermoresistive thin-film sensors and type N thermocouples. Uncoated cemented carbide inserts of the type CCMW120404 were coated by physical vapor deposition (PVD) with a thin-film sensor system for measuring the temperatures in the tool-chip interface as published in previous own works [8]. Aluminum oxide (Al_2O_3) was deposited with a thickness of $4\ \mu\text{m}$ as an insulation layer. Sensor structures made of a 100 nm chromium layer were structured by a combination of photolithography and wet-chemical etching. The thin-film system was completed by a $2\ \mu\text{m}$ thick Al_2O_3 insulation and

wear-protection layer as shown in Fig. 1(a) and Fig. 1(b). The sensor calibration showed a linear response to temperature changes up to 200°C with a sensitivity of about $\alpha = 1.3 \cdot 10^{-3}\ 1/\text{K}$ for $T_0 = 0^\circ\text{C}$ as shown in Fig. 1(c). Cavities were manufactured in both cutting tool and workpiece using electrical discharge machining for placing Type N thermocouples of diameter 0.5 mm. Signals were acquired using a data logger USB-TC from Measurement Computing© placed close to the cutting tool and a wireless encapsulated mini data logger 160-IP 67 from MSR© placed inside the workpiece turning chuck.

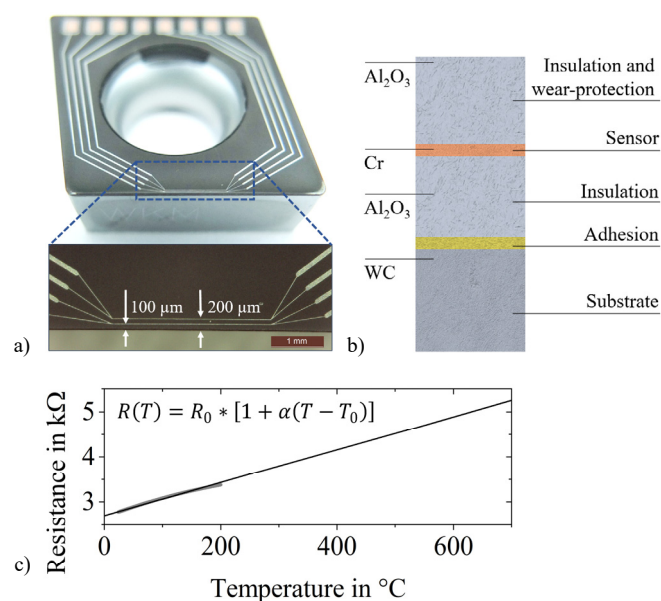


Fig. 1. (a) Temperature sensor design; (b) thin-film system layers; (c) calibration characteristic of one sensor.

Off-machine. The microstructure of the workpiece was analyzed using a Focused Ion Beam (FIB) system combined with Scanning Electron Microscopy (SEM). Micro-perforations were performed in the longitudinal direction of the workpieces. A thin layer of platinum was deposited on the surface of the workpiece close to the perforated area to protect the surface during ion “milling” and from edge rounding.

A micro tester was used for hardness measurements HV 0.005 with a force of 5 g during 10 s. This test load was chosen to realize small indentation, which is necessary to measure within layers, whose thickness may not exceed $10\ \mu\text{m}$. As shown in Fig. 2, Vickers hardness was tested by three indentation rows on each workpiece on two sides, i.e. the hardness-depth-profiles result of six repetitions.

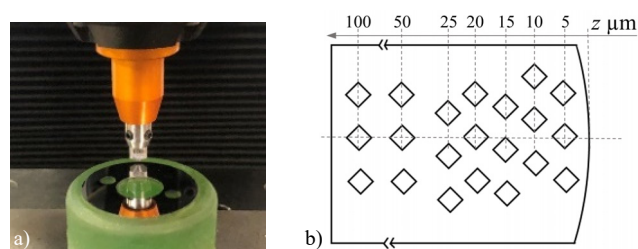


Fig. 2. (a) Qness micro tester with sample; (b) indentation pattern.

2.3. Methods

Finite Element Method (FEM) was used to simulate the chip formation process using the commercial software Simufact Forming 21.0 based on MSC Marc. The simulation featured an Arbitrary-Lagrange-Eulerian (ALE) formulation with workpiece remeshing. The flow stress calculation was carried out using the Johnson-Cook model [9]. The model parameters are given in Table 2, where A is the yield strength, B is the hardening modulus, C is the strain rate sensitivity coefficient, n is the hardening coefficient and m is the thermal softening coefficient.

Table 2. JC-material model parameters

| A in MPa | B in MPa | C | n | m |
|------------|------------|-------|------|-------|
| 595 | 580 | 0.023 | 1.03 | 0.133 |

Supervised learning approaches based on linear regression analysis were performed using Python to model the relationships between a dependent variable, surface hardness, and several independent variables as process parameters and grain size from data sets created from the combination of experimental measurements and FE simulation results.

3. Experimental setup

Dry orthogonal turning tests were conducted on a NC vertical turning machine Index V100. The set up features a static tool while a clamped workpiece rotates and moves towards the tool as shown in Fig. 3 (a). The circular blank specimen were turned from an initial diameter D_o of 49 mm to a final diameter D_f of 30 mm. New tool inserts were used for each test to neglect the tool wear effect. Cutting edge radius r_β of $50 \pm 5 \mu\text{m}$ were measured after the coating process. Rake and clearance angles were set to 0° and 7° respectively. Figure 3 (b) shows a detailed view of the thin film sensor position and the thermocouples on the cutting tool and workpiece. Thermomechanical stresses and their effect on microstructure and surface hardness were full factorial studied by changing the cutting speed v_c from 50 to 300 m/min and the uncut chip thickness h from 10 to $100 \mu\text{m}$ as summarized in Fig. 4 (a). Cutting forces and temperatures measured during the process are shown in Fig. 4 (b).

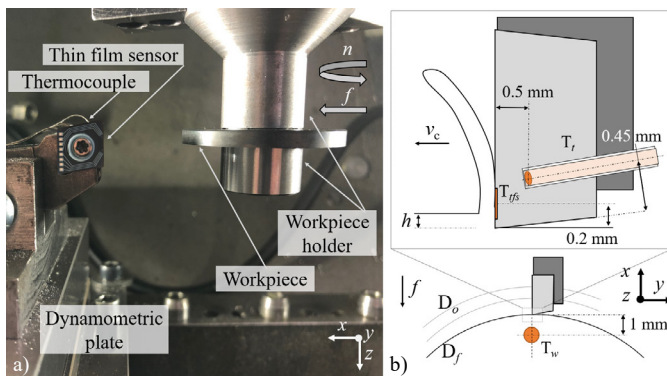


Fig. 3. (a) Experimental setup; (b) detailed view of the cutting tool and workpiece with the position of the thin-film sensors not shown to scale T_{fs} and thermocouples T_t and T_w .

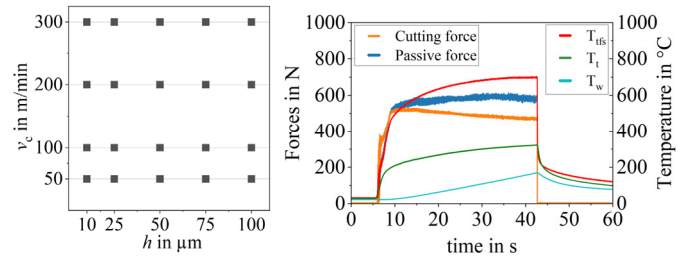


Fig. 4. (a) Full factorial design of experiments; (b) example of force and temperature measurements ($v_c = 100 \text{ m/min}$, $h = 25 \mu\text{m}$).

4. Numerical modelling

2D FEM simulations were carried out to obtain temperatures and stresses distribution in the workpiece. The model was set up with a mesh type quadrilateral elements with a plain strain assumption and implicit time integration. The simulation featured a rigid tool fixed in the space, an elasto-plastic workpiece, a heat sink and the measured temperatures as fixed bodies as shown in Fig. 5. A two-step approach was carried out to minimize the simulation time for each process parameter combination.

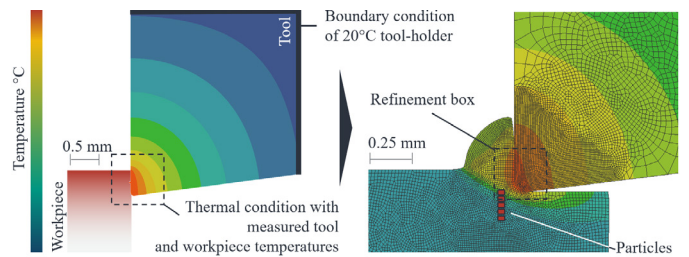


Fig. 5. 2D finite element process model of orthogonal cutting.

In the first step, the tool and workpiece temperatures were set according to the measured temperatures at the end of the test by the thin film sensors (T_{fs}) and the workpiece thermocouple (T_w). The temperature distribution and heat partitioning was calibrated using the thermocouple in the cutting tool (T_t). Then, the simulated tool and workpiece thermal distributions were integrated into a chip formation simulation as shown in Fig. 5.

In the second step, a cutting simulation of cutting path 5 mm was performed using the same mesh type with continuous remeshing depending on refinement boxes featuring local refinement under the cutting tool. This approach leads to time efficient FE simulations since large mesh displacements are reduced to a minimum. The friction of the system was described using a temperature independent and combined Coulomb-shear friction model. The Coulomb factor value μ and the shear factor value m were fixed at 0.35 and 0.70. Results were validated using the measured temperature and force values.

Starting from the workpiece surface according to Table 3, the temperatures and stress profiles were extracted by the means of particle-tracking at the end of the simulated cutting path.

Table 3. Particle tracking

| Particle number | 1 | 2 | 3 | 4 | 5 | 6 | 7 | 8 |
|---------------------------|---|----|----|----|----|----|----|-----|
| Distance in μm | 5 | 10 | 15 | 20 | 25 | 30 | 50 | 100 |

5. Results

5.1. Forces, temperatures and stresses

The measured cutting forces and punctual temperatures on tool and workpiece are used to calibrate the FE simulations and to model the surface hardening empirically. Figure 6 shows the cutting and passive forces and the temperatures T_t measured during the experiments. Forces increase directly proportional to increase in cutting speed and uncut chip thickness. Cutting edge radius size effect is intensified for uncut chip thickness values less than $h = r_\beta = 50 \mu\text{m}$. Chip formation becomes irregular and lead to higher ploughing forces and workpiece surface temperature as well as a dynamically unstable process with chatter appearance (e.g. $v_c = 300 \text{ m/min}$, $h = 25 \mu\text{m}$).

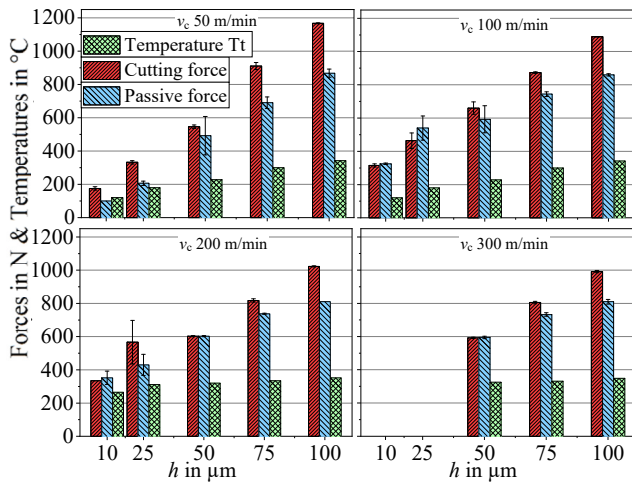


Fig. 6. Cutting forces and tool temperatures T_t measured during the tests.

Figure 7 shows an example of workpiece surface temperatures and stress gradients obtained from the FE simulations using the tracking particles from Table 3. The closest points to the workpiece surface at a distance of $5 \mu\text{m}$ show temperatures up to 600°C for aggressive cutting speeds and 500°C for more conservative conditions, in any case far from the austenitization temperature of 855°C . As a result, stresses show a compressive character rather than a tensile character, which is due to the predominance of thermal contraction and compressive forces against microstructural changes. At high v_c , stress relaxation is more abrupt, resulting in greater changes in character from compression to tension. These results are combined with the measured hardness profiles to look for dependency relationships.

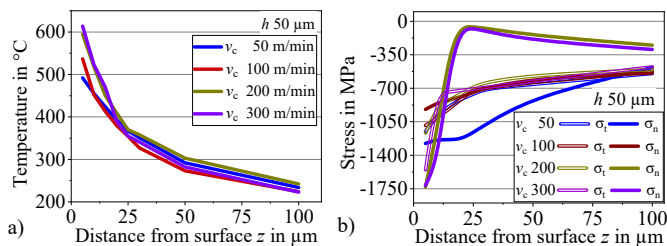


Fig. 7. Example of FE simulated (a) temperature and (b) stresses profiles.

5.2. Microstructure gradient analysis

Grain microstructures closer to the surface undergo dynamic recrystallization generating nano-size structures because to the thermal and mechanical loads. Figure 8 shows the characteristic FIB capture where three sections can be identified. The first section results from the combination of severe plastic deformations (SPD), high thermal gradients. Consequently, the grains were recrystallized and finally refined giving rise to an ultrafine grain (UFG) layer $Z_{gs<100\text{nm}}$ with grain sizes below 100 nm . Grain phase transformations do not occur in this material and heat treatment state. Below this layer, a microcrystalline sheared layer with a grain size less than $1 \mu\text{m}$ conforms the second section. A plastic deformed transition area to bulk material corresponds to the third section.

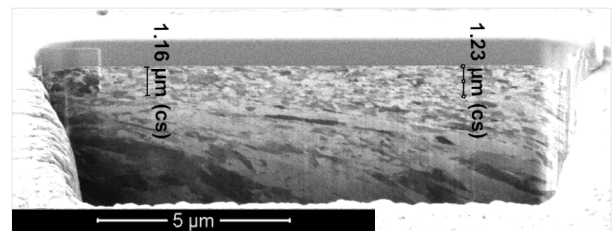


Fig. 8. Microstructure evolution and thickness of nanocrystalline layer.

The thickness of the nanocrystalline layer $Z_{gs<100\text{nm}}$ was measured and the results of the grain evolution are shown in Fig. 9 and Fig. 10. The formation of ultrafine grains depends directly on the temperatures and forces generated during the cutting process. In Fig. 6 was shown how the cutting forces F_c increase at thicker h and decrease at higher cutting speeds due to an increment of the process temperature when $h > r_\beta$. However the thickness of $Z_{gs<100\text{nm}}$ does not increase directly with the process forces, as could be expected.

To correctly interpret Fig. 10, Fig. 9 should also be considered. Surface temperatures $T_{z=5\mu\text{m}}$ were obtained from the FE simulations and combined with the experimental values of the cutting forces and compared with the thickness of $Z_{gs<100\text{nm}}$. It has been observed, that higher temperatures accompanied with higher forces lead to thinner nanocrystalline layers. In order to explain this non-intuitive phenomenon the ratio between F_c and F_p has to be considered introducing a new parameter $\alpha_f = F_c / F_p$. A smaller α_f indicates relatively more significant passive forces with respect to cutting forces, leading to the generation of a thicker recrystallized grain layer. Temperature contributes to the nanocrystalline layer formations and will be investigated in the next section.

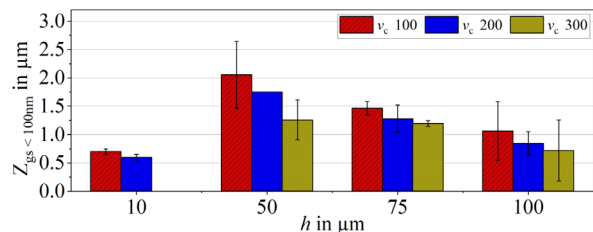


Fig. 9. Nanocrystalline layer thickness dependency on process parameters.

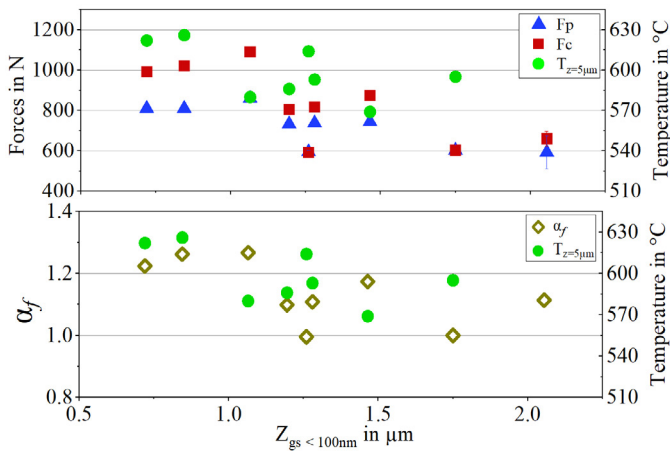


Fig. 10. Nanocrystalline layer thickness dependency on cutting forces and surface temperature obtained from FE simulations.

5.3. Microhardness analysis and modelling

The generation of thermally induced white layers is improbable during turning of AISI4140 QT 600 since the achievable temperatures on the workpiece are not high enough. Therefore a possible hardness increase is caused by work hardening and grain refinement, but not by phase transformation.

As observed with the FIB measurements the affected surface layer corresponds to few micrometers 5–10 μm. The effect of the cutting conditions on the surface hardness is shown in Fig. 11. It can be seen that at low and high cutting speeds, v_c 50 and 300 m/min, the workpiece undergoes mainly hardening phenomena. However, when $h < r_\beta$ the predominant phenomenon is softening.

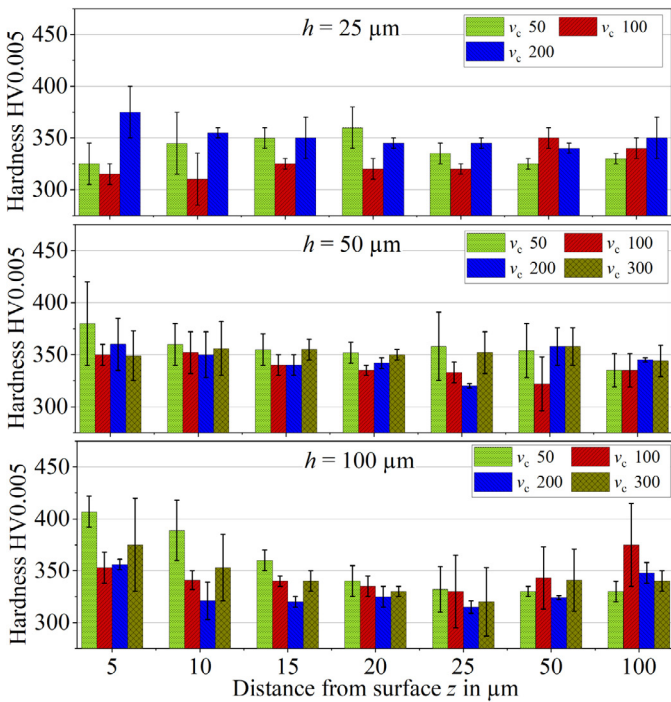


Fig. 11. Measured surface hardness evolution.

The influence of process parameters and thermomechanical loads on surface hardening and softening have been investigated and modelled with the aid of regression analysis. The modelling strategy is summarized in Table 4 and assumes the surface hardness evolution as linear. This simplification takes the surface hardness value HV as dependent variable and looks forward finding the optimal independent variables. These variables have been obtained in the experiments and from the simulations leading to empirical and hybrid models. The database with the values of the independent variable was split into training, 80%, and validation, 20% of the data. The coefficient of determination R^2 is the proportion of the variation in the dependent variable that is predictable from the independent variable and it will be used to express the quality of the model. The model coefficients have been obtained with the ordinary least squares method.

First, the surface hardness value is modelled as a linear function of the process parameters v_c and f . This approach does not need in-process measurements and neglects many factors that influence the surface hardness, e.g. the cutting edge microgeometries.

The second approach uses the information acquired during the cutting process: F_p , F_c and T_{fs} . This lead to more accurate predictions since the thermomechanical loads are directly considered, as well as indirectly the size effect, tool wear, etc. This dependent variables offer the most accurate model. The variable with more importance for the model is F_p , followed by the temperature and F_c . The main inconveniency is the collinearity that these variables present, which in some cases can lead to very inaccurate predictions. In the approaches III-V the thermomechanical loads were combined with the process parameters, with the nanocrystalline thickness $Z_{gs < 100nm}$, however the models showed less accuracy. It is remarkable the strong non-linearity of $Z_{gs < 100nm}$ with HV, which notably minimize the accuracy of the model.

Table 4. Linear regression based surface hardness modelling strategies

| Linear regression | |
|---|---|
| $HV = w_0 + w_1 v_c + w_2 f$ $R^2 = 0.29$ | $HV = w_0 + w_1 F_c + w_2 F_p + w_3 T_{fs}$ $R^2 = 0.53$ |
| | |
| $HV = w_0 + w_1 F_c + w_2 F_p + w_3 v_c + w_4 f$ $R^2 = 0.37$ | |
| $HV = w_0 + w_1 F_c + w_2 F_p + w_3 v_c + w_4 f + w_5 T_{fs}$ $R^2 = 0.38$ | |
| $HV = w_0 + w_1 F_c + w_2 F_p + w_3 v_c + w_4 f + w_5 Z_{gs < 100nm}$ $R^2 = 0.15$ | |
| $HV = w_0 + w_1 \sigma_n + w_2 \sigma_t + w_3 T_z + w_4 z; \quad z : 0 \text{ to } 100 \mu m$ $R^2 = 0.40$ | |

The sixth approach uses the results from the FE simulations: temperature and stress gradients T , σ_n and σ_t , and the experimental values of the hardness depending on the depth Z . Therefore not only one value of the surface hardness is predicted, but its evolution over the sub-surface. This method turned out to be the second most effective, but it also suffers from strong collinearity. Once the dependent variables that best represent surface hardness were determined, other linear approaches were investigated. Table 5 shows three approaches consisting of quadratic and logarithmic regression. The accuracy of the models is greatly increased compared to first-order approaches. The relationship between F_p and F_c , α_f , presented in the previous chapter has been used to minimize the collinearities of the independent variables. The approach based on quadratic regression using α_f and the temperature measured with the thin film sensors offers the highest accuracy for predicting the surface hardness. A model can be considered with an R^2 greater than 0.75 that significantly represents the dependent variable. However, in all the data-driven methods, the accuracy of the model depends directly on the quality of the training data. In this case, the training data: the surface hardness values HV0.005 present a quite wide standard deviation, which must be considered when calculating the real accuracy of the model and added as a term ε to the function. This error leads more inaccurate model predictions and is common to all the modelling approaches.

Table 5. Other regression approaches

| |
|---|
| Quadratic regression |
| $HV = w_0 + w_1 F_c + w_2 F_p + w_3 T_{tfs} + w_4 F_c^2 + w_5 F_p^2 + w_6 T_{tfs}^2$ |
| $w_0 = -1e6; w_1 = 90; w_2 = -30; w_3 = 500$ |
| $w_4 = \sim 0; w_5 = 0.02; w_6 = -0.04$ |
| $R^2 = 0.69$ |
| Logarithmic regression |
| $HV = w_0 + w_1 F_c + w_2 F_p + w_3 T_{tfs} + w_4 \ln(F_c) + w_5 \ln(F_p) + w_6 \ln(T_{tfs})$ |
| $w_0 = -1e6; w_1 = -15; w_2 = 430; w_3 = -150$ |
| $w_4 = 15e3; w_5 = -30e3; w_6 = 1e5$ |
| $R^2 = 0.82$ |
| Quadratic regression with reduced collinearity |
| $HV = w_0 + w_1 \alpha_f + w_2 T_{tfs} + w_3 \alpha_f^2 + w_4 T_{tfs}^2$ |
| $w_0 = 2e3; w_1 = 1500; w_2 = -10; w_3 = -650; w_4 = 0.008$ |
| $R^2 = 0.76$ |

6. Conclusion

Surface hardness and microstructures of AISI 4140 workpieces has been investigated and modelled using different regression strategies. The key findings of this work are:

- Passive forces, followed by temperature gradients, cutting forces and cutting edge are the parameters that affect more significantly the surface hardening in this case.
- High temperatures and forces did not lead in all cases to more surface hardening. However the forces ratio α_f

combined with the temperature can be used to predict the grain refinement and the nanocrystalline layers.

- The strong collinearity between the independent variables must be considered to assess the accuracy of the model.
- A correlation between recrystallized grain layer and hardened surface is not linear and it has been shown not to be the best strategy for modeling surface hardness.
- FE simulations can be combined with experimental values of surface hardening in order to create hybrid models that estimate the hardness evolution in the sub-surface. This is very interesting when the surface hardness behaves as a polynomial function with softening and hardening trends.
- The best modelling approach for surface hardening studied in this work is the logarithmic regression using the forces and temperatures.

Once the independent variables that better describe the surface hardness are identified, other functions and fitting strategies have to be investigated, e.g. more complicated polynomial functions combined with machine learning-based fitting approaches.

Acknowledgements

The scientific work has been supported by the DFG within the research priority program SPP 2086 and SPP 2231. The authors thank the DFG (SCHU 1010/63-1), (BR 2178/47-1) and (SCHU 1010/75-1) for this funding and intensive technical support.

References

- [1] Kocks UF, Mecking H. Physics and phenomenology of strain hardening: the FCC case. *Prog Mater Sci.* 2003; 48:171–186.
- [2] Zhang, F. Y., Duan, C., Sun, W., Ju, K. Influence of white layer and residual stress induced by hard cutting on wear resistance during sliding friction, *Journal of Materials Engineering and Performance*, 2019; 28:7649–7662.
- [3] Hosseini S.B., Klement U. A descriptive phenomenological model for white layer formation in hard turning of AISI 52100 bearing steel. *CIRP Journal of Manufacturing Science and Technology* 2021; 32:299–310.
- [4] Estrin, Y., Toth, L. S., Molinari, A., and Brechet, Y., A dislocation-based model for all hardening stages in large strain deformation, *Acta Materialia*, 1998; 46, pp. 5509–5522.
- [5] Ding H, Shin YC. Dislocation density-based grain refinement modeling of orthogonal cutting of titanium. *ASME. J. Manuf. Sci. Eng.* 2014; 136:041003-11.
- [6] Ambrosy F, Zanger F, Schulze V. FEM-simulation of machining induced nanocrystalline surface layers in steel surfaces prepared for tribological applications. *CIRP Annals- Manufacturing Technology* 2015; 64:69-72.
- [7] Hänel A, Seidel A, Frieß U, Teicher U, Wiemer H, Wang D, Wenkler E, Penter L, Hellmich A, Ihlenfeldt S. Digital twins for high-tech machining applications — A model-based analytics-ready approach. *Journal of Manufacturing and Materials Processing.* 2021; 5(3):80.
- [8] Plogmeyer M, González G, Schulze V, Bräuer G. Development of thin-film based sensors for temperature and tool wear monitoring during machining. *tm-Technisches Messen.* 2020; 87(12): 768-776.
- [9] Johnson GR, Cook WH. Fracture characteristics of three metals subjected to various strains, strain rates, temperatures and pressures. *Engineering Fracture Mechanics* 21 (1), 1985: 31-48.